J. Fluid Mech. (2009), *vol.* 625, *pp.* 273–298.
doi:10.1017/S0022112008005697 Printed in the United Kingdom

Computational study of optical distortions by separated shear layers and turbulent wakes

ALI MANI[1]†, PARVIZ MOIN[1] AND MENG WANG[2]

[1]Center for Turbulence Research, Stanford University, CA 94305, USA

[2]Department of Aerospace and Mechanical Engineering, University of Notre Dame, IN 46556, USA

(Received 29 February 2008 and in revised form 15 December 2008)

The flow over a circular cylinder at $Re_D = 3900$ and 10 000 and $M = 0.4$ is considered a platform to study the aero-optical distortions by separated shear layers and turbulent wakes. The flow solution is obtained by large eddy simulation (LES) and validated against previous experimental and numerical results. The fluctuating refractive index obtained from LES is used in a ray-tracing calculation to determine wavefront distortions after the beam passes through the turbulent region. Free-space propagation to the far field is computed using Fourier optics. The optical statistics are analysed for different conditions in terms of optical wavelength, aperture size and the beam position. It is found that there exists an optimal wavelength which maximizes the far-field peak intensity. Optical results at both Reynolds numbers are compared. The optical distortion by the downstream turbulent wake is found to be Reynolds number insensitive. However, due to their different transition mechanisms, distortions by the near wake regions are different in the two flows. The aero-optical effects of different flow scales are examined using filtering and grid refinement. Through a grid convergence study it is confirmed that an adequately resolved LES can capture the aero-optics of highly aberrating flows without requiring additional subgrid scale model for the optics.

1. Introduction

Optical aberrations induced by fluctuations of refractive index in turbulent flows are a serious concern in airborne communication and imaging systems. For air and many other fluids, the refractive index is linearly related to the density of the fluid through the Gladstone–Dale relation, and therefore density fluctuations are the root cause of optical aberrations. An airborne optical beam generally encounters two distinct turbulent flow regimes: the turbulence in the vicinity of the aperture and atmospheric turbulence. Aero-optics is the study of optical distortions due to near aperture turbulent flows, typically involving turbulent boundary layers, free shear layers and wakes (see Gilbert 1982).

When an initially planar optical wavefront passes through a compressible flow, different parts of the wavefront experience different density in the medium and hence have different propagation speeds. Therefore, the beam experiences a wavefront

† Email address for correspondence: alimani@stanford.edu

deformation which can be expressed as (see Sutton 1985; Tromeur *et al.* 2003)

$$\mathscr{L}(x, y) = \int_{z_0}^{z_1} n(x, y, z)\, \mathrm{d}z, \tag{1.1}$$

where n is the refractive index; z is the direction of optical propagation; z_0 and z_1 represent the boundaries of the turbulence region; and $\mathscr{L}$ is referred to as the optical path length (OPL) which is proportional to the time of travel between z_0 and z_1 for individual rays. Wavefront distortion can be described in terms of variations of $\mathscr{L}$ about its mean:

$$OPD(x, y) = \mathscr{L}(x, y) - \overline{\mathscr{L}}, \tag{1.2}$$

where OPD is the optical path difference, and the bar symbol represents planar averaging. For a single-frequency optical beam with wavelength λ , the optical phase distortion associated with $\mathscr{L}$ will be $2\pi OPD/\lambda$. An initial phase distortion can lead to large errors in the far field. The consequences of such deformations include optical beam deflection, beam spread and loss of intensity.

Since optical distortions are present at high spatial and temporal frequencies, probing their corresponding mechanisms is a challenging task. Several experimental investigations have been performed to improve understanding of the phenomena and provide guidelines to control optical distortions. These efforts are mostly aimed at developing high-speed wavefront sensors (e.g. Malley, Sutton & Kincheloe 1992; Hugo *et al.* 1997), studying shear layer interfaces and refractive index structures (e.g. Dimotakis, Catrakis & Fourguette 2001; Catrakis *et al.* 2002; Catrakis & Aguirre 2004), examining optical importance of different length scales (e.g. Zubair & Catrakis 2007), providing empirical models and scaling laws for prediction of optical distortions (e.g. Dimotakis *et al.* 2001; Gordeyev *et al.* 2003) and investigating control techniques to modify aero-optical effects (e.g. Freeman & Catrakis 2008).

Since the late 1980s, numerical studies of aero-optical phenomenon have been employed to complement experiments. Earlier computational approaches typically involved two-dimensional Navier–Stokes solutions. Cassady, Birch & Terry (1989) obtained unsteady two-dimensional solutions for compressible flow over a cavity and analysed its induced optical distortion. Tsai & Christiansen (1990) solved two-dimensional Euler equations for a free shear layer and studied the effects of flow forcing on optical distortions. More elaborate approaches involved Reynolds-averaged Navier–Stokes (RANS) calculations using a turbulence model such as the k-ε model. Algebraic relationships were then used to obtain the root mean square (r.m.s.) of intensity and length scales of the index of refraction field. Smith & Truman (1990) solved a model transport equation for the r.m.s. refractive index fluctuations. The turbulence information was then fed into an optics model based on geometric optics, which predicts properties of the beam such as amplitude loss and spreading. Truman & Lee (1990) and Truman (1992) were among the first to perform time-accurate computational studies of aero-optical distortions. They used direct numerical simulation (DNS) of a homogeneous shear flow and turbulent channel flow to study the induced optical wavefront errors. The simulations were based on incompressible flow equations at relatively low Reynolds numbers, and the fluctuating refractive index was modelled by a passive scalar.

Because of its ability to resolve fluid motions over a wide range of scales at a reasonable computational cost, large eddy simulation (LES) has emerged as a modern tool for aero-optical predictions. Childs (1993) carried out LES of a compressible turbulent mixing layer and performed ray tracing through it. Jones

& Bender (2001) used LES to study aero-optical distortions in a fuselage/turret configuration. Tromeur *et al.* (2003) and Tromeur, Garnier & Sagaut (2006) used LES to study aero-optics of transonic and supersonic boundary layers. They compared their directly computed phase distortion variance with that obtained from Sutton's (1969) model and concluded that Sutton's model cannot accurately capture phase distortion variance of the boundary layer. Sinha *et al.* (2004) used experiments and LES to investigate control of flow fields to mitigate the distortion of a laser beam passing through a cavity shear layer. Visbal & Rizzetta (2008) used LES to study aero-optics of a free shear layer and examined effects of flow excitation on delaying the roll-up of the shear layer and reducing its consequent optical distortion.

The optical phase distortion magnitude ($|2\pi OPD/\lambda|$) in these studies varies from case to case. This quantity can be as low as $O(0.1)$ for a boundary layer flow (see, for example, Tromeur *et al.* 2003) or as high as $O(10)$ for a compressible wake flow (e.g. Jones & Bender 2001).

Depending on their phase distortion magnitude, different methods can be used to describe the far-field optical quality of distorted beams. Mahajan (1983) carried out an analysis for the case of small phase distortions and suggested that the ratio of the maximum far-field optical intensity to that of an undistorted beam, called the Strehl ratio (SR), is a direct function of the r.m.s. of the phase distortion variance:

$$SR = \max(I)/\max(I_{undistorted}) = \exp(-(2\pi OPD_{r.m.s.}/\lambda)^2). \tag{1.3}$$

Once the optical phase distortion is computed (using (1.1)), this estimate can be used to describe the far-field beam quality without directly computing the far-field optical intensity. However, this method is limited to small phase distortions.

Mani, Wang & Moin (2006) recently performed an analysis of highly distorted beams and introduced a new set of metrics describing the far-field distortions based on the moments of the optical intensity pattern. Their measures have provable scaling properties with key parameters such as optical wavelength and distance of propagation. In addition, effects of diffraction and flow-induced distortions are decoupled in their metrics. These properties make their measures a suitable tool for studying aero-optics of highly distorted beams.

The first objective of this work is to study aero-optical distortions due to separated shear layers and highly aberrating wake flows by computing the relevant far-field optical statistics and their relations with the underlying aberrating flow. Some of these statistics are based on the measures described by Mani *et al.* (2006). In addition, statistics based on time-averaged irradiance are computed, and their dependence on parameters such as optical wavelength and the aperture size are explored.

The second objective of this study is to assess the capability of LES to capture the aero-optical effects of the wake flow with high fidelity, particularly the effects of different flow scales. Most of the previous LES-based aero-optical computations used dissipative numerical schemes, which artificially damp small resolved scales of the flow (see Mittal & Moin 1997 for details). The work by Tromeur *et al.* (2003) is an exception in which accuracy of the aero-optical computation for a boundary layer flow is verified through a grid convergence study. Since wake flows involve higher magnitudes of optical phase distortions, capturing all of the relevant flow scales is even more challenging.

The paper is organized as follows. In the next section, the LES methodology employed for flow simulation is described, and flow statistics obtained from the computations are compared to results of the previous studies to validate the simulations. In § 3 optical configurations are described, and the methods for optical

computations are presented. Instantaneous optical results are shown in § 4. Section 5 presents the optical statistics and discusses the effects of optical parameters and flow features on these statistics. Section 6 compares the flow fields at $Re_D = 10\,000$ with that at $Re_D = 3900$ and contrasts their induced optical distortions. In § 7 the effect of small-scale flow structures on optical statistics is examined, and the results of a grid convergence study are discussed. Conclusions are presented in § 8.

2. Flow simulation

We computed three-dimensional compressible flow over a circular cylinder at Reynolds numbers 3900 and 10 000 based on cylinder diameter. Computations are performed using a sixth-order LES code, developed by Nagarajan, Lele & Ferziger (2003), which is based on conservative compact finite difference on staggered mesh. The time advancement scheme is second-order implicit near the wall and third-order Runge–Kutta away from the wall. The dynamic subgrid scale (SGS) model for compressible flow by Moin *et al.* (1991) with modification of Lilly (1992) is used to account for the effect of the unresolved structures on the flow. The discretization of the code is based on a generalized curvilinear coordinate formulation. More details on the numerical scheme are presented in Nagarajan *et al.* (2003).

The computational domain has a radius of approximately $35D$ ($D =$ cylinder diameter) and a width of πD in the spanwise direction. The mesh size is $288 \times 396 \times 48$ in the wall normal, azimuthal and spanwise directions, respectively, totalling about 5.5 million grid points. The wall normal grid spacing at the leading edge is $0.00062D$ with maximum grid stretching of 4 %. A 'sponge' layer with thickness of $15D$ is applied at the outer boundary to damp out the flow features exiting the domain and making the boundary non-reflecting. The same mesh is used for simulations at both Reynolds numbers in order to avoid mesh-biased conclusions when studying the effect of Reynolds number. The grid independence of the results is discussed in § 7.

The total integration time was over 60 cycles of vortex shedding for the $Re = 3900$ case and over 30 sheddings for the $Re = 10\,000$ case. In the $Re = 3900$ case, 1400 snapshots of the density field were uniformly sampled from the last 46 shedding cycles (one snapshot per 50 time steps) for subsequent aero-optical study. Similarly, the last 15 shedding cycles of the high-Reynolds-number flow were used for aero-optical investigations.

The literature includes several numerical and experimental investigations of flow over cylinder which can be used to validate our flow computations. For each Reynolds number we performed two separate flow simulations, one at Mach number 0.2 and the other at Mach number 0.4. Since all of the previous studies of this flow are based on incompressible flow regime, the Mach 0.2 simulation was used to validate the computations, and the Mach 0.4 simulation was used for the aero-optical computations.

Table 1 compares the major flow statistics from our simulations with the previously published results. For the case of Mach 0.2 the global statistics are consistent with other studies. At Mach 0.4 there is a notable difference in the drag coefficient, which is attributed to the effect of compressibility. Figure 1 presents the wake profiles of the mean velocity and the Reynolds normal stress components in the streamwise and cross-flow directions in comparison to previous studies. The present results agree well with the LES results of Kravchenko & Moin (1998) and reasonably well with the experimental data of Ong & Wallace (1999) except at the first station. The velocity

	C_d	$-C_{p_b}$	St	θ_{sep}	U_{min}
Experiments[a]	0.99 ± 0.05	0.88 ± 0.05	0.215 ± 0.005	86 ± 2	-0.24 ± 0.1
LES[b]	1.00	0.95	0.203	85.8	−0.32
LES[c]	1.00	0.93	0.207	86.9	−0.35
LES[d]	1.04	0.94	0.210	88.0	−0.37
LES[e]	0.97	0.85	0.213	88.2	−0.31
Present, $M = 0.2$	0.99	0.86	0.206	86.3	−0.33
Present, $M = 0.4$	1.17 ± 0.01	1.05 ± 0.01	0.200 ± 0.002	87.1	-0.27 ± 0.01

[a] Referenced by Kravchenko & Moin (2000)
[b] Beaudan & Moin (1994)
[c] Mittal & Moin (1997)
[d] Kravchenko & Moin (2000, 1998)
[e] Rizzetta, Visbal & Blaisdell (2003)

TABLE 1. Comparison of global flow statistics for flow over a circular cylinder at $Re = 3900$. The parameters from left to right are drag coefficient, base pressure coefficient, Strohal number of vortex shedding, separation angle and minimum averaged streamwise velocity.

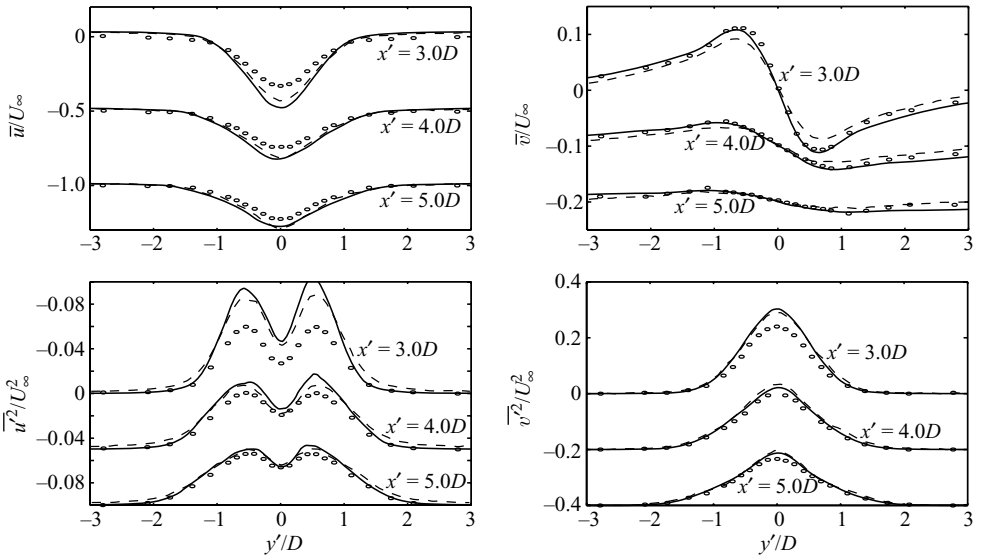

FIGURE 1. Mean and variance of the velocity field at three stations in the wake of the cylinder at $Re = 3900$: u is the velocity in the streamwise direction (x') and v is the velocity in the cross-flow direction (y'); ———, present LES ($M = 0.2$); – – – –, LES of Kravchenko & Moin (1998); ○, experiment (Ong & Wallace 1999).

at this station is sensitive to the location of the shear layer breakdown, which is, in turn, sensitive to free-stream conditions as well as numerical errors. Figures 2 and 3 compare the wake profiles obtained from present simulations with the experimental measurements by Dong *et al.* (2006).

Figure 4 shows the energy spectra of the vertical velocity in the wake centreline five diameters behind the cylinder. The present simulation successfully captures the details of the experimental spectrum, including high-frequency components

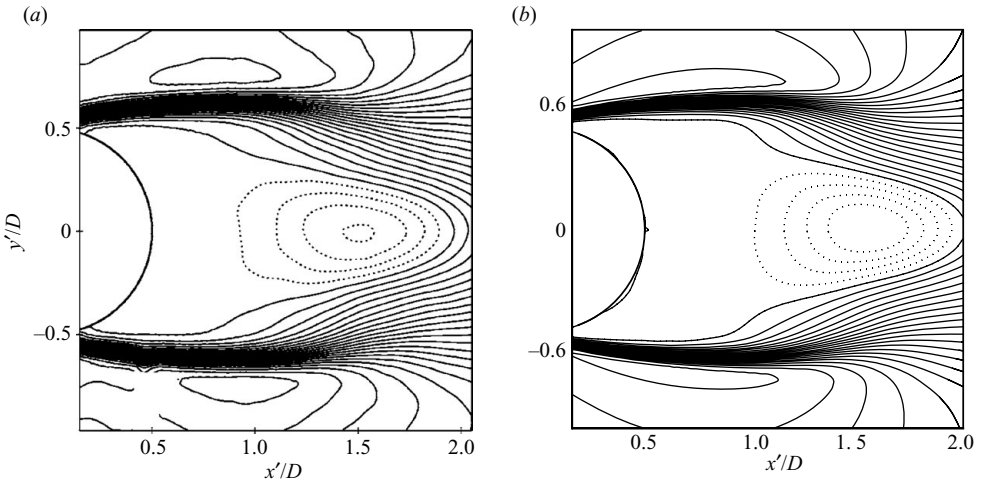

FIGURE 2. Contours of mean streamwise velocity at $Re = 3900$. (*a*) Experiment of Dong *et al.* (2006) ($Re = 4000$); (*b*) present LES at $M = 0.2$. In both plots $\overline{u}_{min}/U_\infty = -0.252$ and $\Delta\overline{u}/U_\infty = 0.063$.

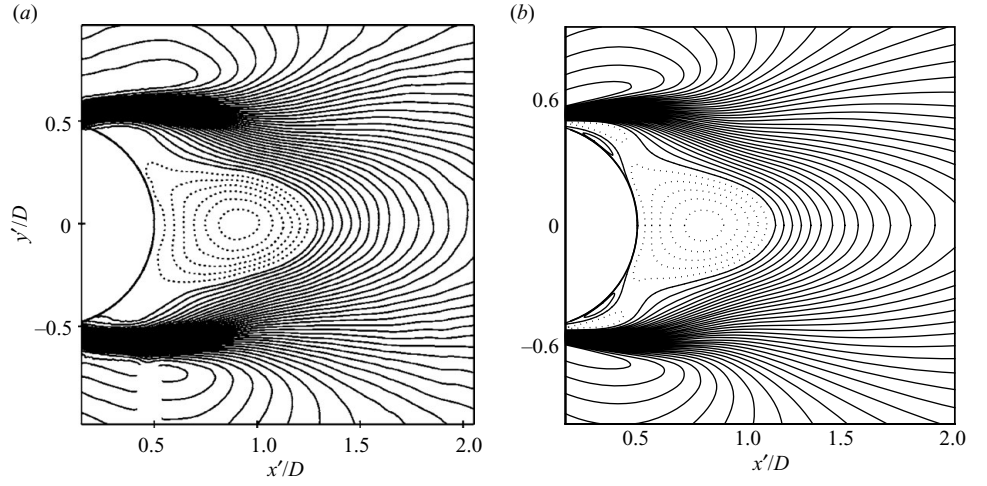

FIGURE 3. Contours of mean streamwise velocity at $Re = 10\,000$. (*a*) Experiment of Dong *et al.* (2006); (*b*) present LES at $M = 0.2$. In both plots $\overline{u}_{min}/U_\infty = -0.228$ and $\Delta\overline{u}/U_\infty = 0.038$.

and the two spectral peaks (at the vortex shedding frequency and its third harmonic).

Table 1 and figures 1–4 confirm that the numerical method employed can capture the global statistics, mean and fluctuating velocity statistics and a wide range of temporal and spatial flow scales. As further evidence of the accuracy of the computed density field, we have validated the simulated sound field against integral solution to the Ffowcs Williams–Hawkings equation. We will present the aeroacoustics results from this flow in another publication.

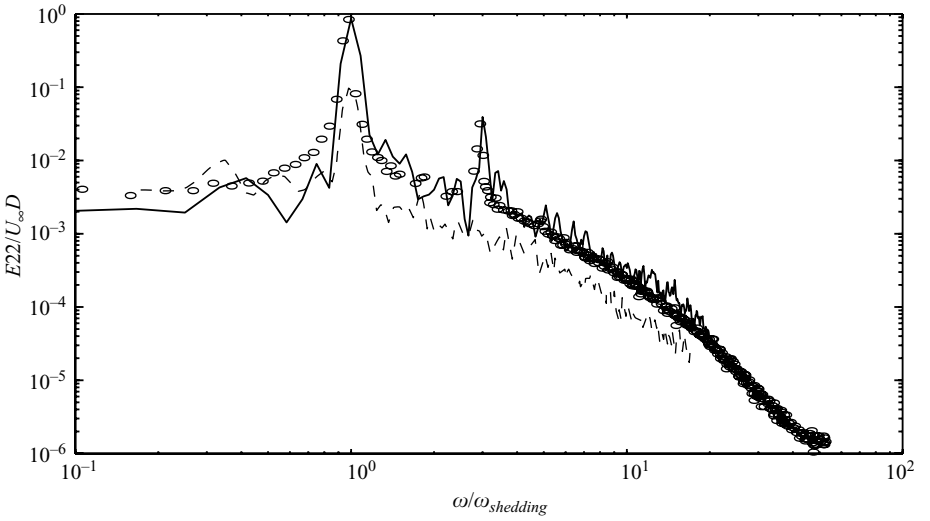

FIGURE 4. Energy spectra of vertical velocity at $x' = 5D$ and $y' = 0$ in the wake of the cylinder at $Re = 3900$: ——— , present LES ($M = 0.2$); – – – – , LES of Kravchenko & Moin (1998); ○, experiment (Ong & Wallace 1999).

3. Optical computation

3.1. *Optical configurations*

In this paper x', y', z' coordinates are used to describe the flow variables, and x, y, z coordinates are designated to describe the optical beam such that z is in the direction of optical propagation and y is aligned with the spanwise flow direction. For optical analysis, six different cases are considered as shown schematically in figures 5 and 6. In the first three cases the optical beams are emitted from the surface of the cylinder. These cases are relevant to practical applications where an optical beam is shot from an optical turret on an airborne vehicle. As shown in figure 5, the first three beams make angles of 17°, 34° and 51° with the downstream flow direction respectively. In cases 2 and 3 the beams pass through the separated shear layer in its transition regime, while in case 1 the beam passes through the turbulent shear layer and a considerable portion of the wake. We did not consider any beam passing through the leading portion of the cylinder, since the corresponding flow region is not optically distorting. Guided by realistic applications, the diameter of the beam is chosen to be $0.3D$. Due to numerical considerations the optical amplitude profile is a Gaussian that extends beyond nominal aperture diameter in each case.

As the flow convects downstream of the cylinder, the turbulent wake grows in size, while the turbulence intensity decays. Case 4 and case 5 are considered to examine the optical effect of turbulence evolution. In these two cases optical beams with the same optical parameters as in the first three cases are shot vertically through the wake of the cylinder. In case 4 the axis of the beam is located at $x' = 1.5D$, and in case 3 it is at $x' = 3.5D$. Finally, in order to examine the effect of aperture size on optical statistics, we considered case 6 in which the diameter of the optical aperture is doubled to $0.6D$, and other parameters are kept the same as in case 5.

3.2. *Numerical considerations*

For optical computations, the propagation domain was decomposed into two regions for each beam: the turbulence region near the aperture and the homogeneous region

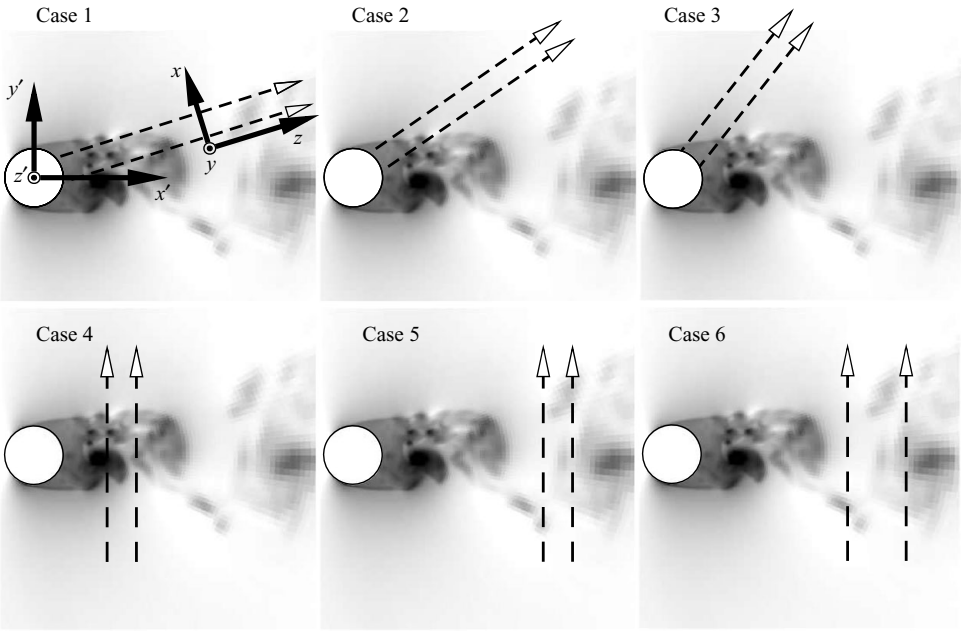

FIGURE 5. Schematics of beam geometry for six different cases. Dashed lines with arrows represent direction of optical propagation. The distance between each arrow pairs shows the diameter of the Gaussian amplitude profile at the optical aperture. The contours show instantaneous density magnitude between $0.8\rho_\infty$ and ρ_∞.

beyond. Each wavefront leaves the optical aperture at $z = z_0$ and then passes the turbulence region between z_0 and z_1 followed by propagation to z_{far}. In the first region the beam passes through the simulated turbulence, and it experiences a wavefront distortion as described by (1.1). The change in the wave amplitude in this region can be ignored, and the electromagnetic field after passing through this region can be computed based on the phase distortion given by (1.1) (see Sutton 1985; Tromeur *et al.* 2003)

$$U(x, y, z_1) = U(x, y, z_0) \exp\left[\frac{-2\pi j \mathscr{L}(x, y)}{\lambda}\right], \tag{3.1}$$

where U is the electromagnetic field; λ is the optical wavelength; and $j = \sqrt{-1}$. In the present study, considering the order of magnitude of density fluctuations in the domain, the length of the first region $(z_1 - z_0)$ is chosen to be $10D$.

A solution based on (1.1) and (3.1) assumes that the beam photons travel along straight lines between z_0 and z_1, and deflection of the beam due to refraction is ignored. In this study, we allowed for beam deflections in the ray-tracing computations, and it was confirmed that the changes due to this modification were in fact small. The maximum beam deflection was about 0.3 % of the cylinder diameter and the maximum far-field intensity change was about 3 % due to this modification.

The amplitude profile of the beam at the aperture is assumed to be

$$\mathscr{A}(x, y) = U(x, y, z_0) = \mathscr{A}_{max} \exp\left(-\frac{x^2 + y^2}{a^2}\right), \tag{3.2}$$

where a is the beam radius, equal to $0.15D$ for cases 1–5 and $0.3D$ for case 6, and $\mathscr{A}_{max}$ is the peak amplitude. To maintain the same optical power for all beams, the

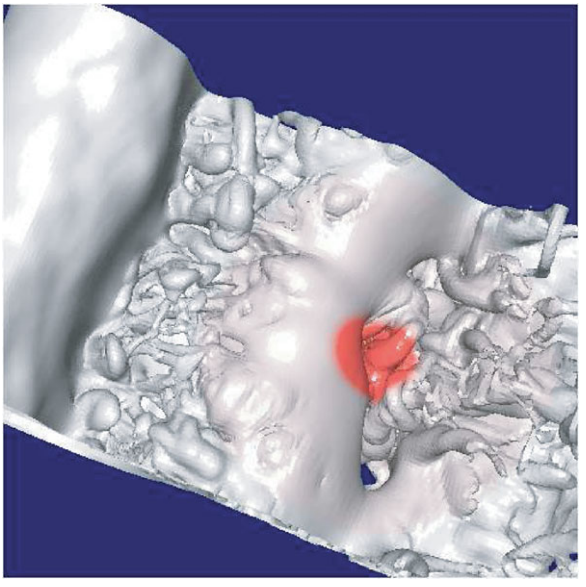

FIGURE 6. Isosurfaces of density $\rho = 0.98\rho_\infty$ at a time instant. The red zone schematically represents the optical beam in case 6.

amplitude of the case 6 beam is half of that in cases 1–5. In the computations, the Gaussian profiles were truncated at $2.25a$ away from the optical axis where the optical intensity (amplitude squared) is less than 0.01 % of the centre value.

The integral in (1.1) is computed in x, y, z coordinates, using the fourth-order Simpson rule. Third-order splines are used to interpolate the density values. Since the ray-tracing coordinates are not aligned to the curvilinear flow coordinates, we used a non-standard interpolation approach to maintain the high-order accuracy of interpolation. According to this method, we required invertible mapping to generate the flow mesh. In addition to the flow mesh, we generated a Cartesian grid in the x, y, z coordinates. We then used the inverse mapping to pre-compute and save the exact curvilinear coordinate of each Cartesian grid point. To look up the density values in the subsequent ray-tracing routines, we first used Cartesian coordinates of each ray as inputs and employed three-dimensional splines (see Press *et al.* 2007) in conjunction with the pre-computed coordinates to obtain the curvilinear coordinates of each ray. Once locating the rays in the density field mesh, we used an additional spline to interpolate the density values.

We note that the OPL distortion due to curvature of the cylinder surface is subtracted from our OPL computations. In other words, we assume that a steady correction is employed to the propagated wavefronts so that they propagate without distortion under no-flow condition ($\rho = \rho_\infty$).

The initial phase distortion by the turbulent region causes subsequent changes of optical intensity in the far field. We used Fourier optics methods to compute the far-field intensity pattern for each case. The Fraunhofer approximation (see Saleh & Teich 1991) is used if the distance of propagation is sufficiently large; otherwise our Fourier optics is based on the exact solution of the wave equation.

We report the estimated statistical error for some of the presented time-averaged quantities. These errors are due to finite sample size and are obtained by comparing the statistics obtained using different time windows. Typically we use windows of

Parameter	Default value	Other values studied
λ/D	2.5×10^{-6}	10^{-5} and 4×10^{-5}
$(z_{far} - z_1)/D$	10^5	2000, 4000, 8000 and 32 000
Aperture diameter $(2a/D)$	0.3	0.6
Optical configuration	Case 1	Cases 2–6
Re	3900	10 000
M	0.4	

TABLE 2. The dimensionless parameters in optical computations.

about six shedding cycles and compute statistics using up to seven non-overlapping windows. Assuming uncorrelated estimates from different windows, standard error of the mean formula is used to estimate the sampling error of time-averaged quantities.

3.3. *Dimensional and dimensionless parameters*

While we present all of the optical results in this paper in terms of dimensionless values, it is helpful to provide an intuitive sense about these numbers by referring to some physical dimensions. In realistic applications turbulence is generated by a bluff body of dimension of about 0.5 m (see Jones & Bender 2001 for example); the size of the aperture is a fraction of the size of the body (20 %–50 %); the wavelength of the optical device is between 1–10 microns (mostly $\sim$1 μm); and the far field of interest is 1–100 km away from the optical device. Consistently, we chose the dimensionless parameters of our computations (see table 2) such that the relative length scales matched those in realistic applications. However, to make the computations feasible we lowered the Reynolds number (physically, higher viscosity for realistic length scale and free-stream velocity and Mach number). Consequences of using lower Reynolds numbers are discussed in § 6.

Table 2 shows the list of dimensionless optical parameters used in the computations. The table lists a default value for each parameter. We also studied effects of variations to each parameter, and these variations are also listed in the table. We use the cylinder diameter, D, to non-dimensionalize all of the length scales. Also all of the far-field intensity values are non-dimensionalized by peak intensity of the default beam (A^2_{max}) before its propagation.

We also used the non-dimensional form of the Gladstone–Dale law to relate index of refraction fluctuations to the computed density field. According to Wolfe & Zizzis (1978) the Gladstone–Dale constant of air for the wavelengths between 1 μm and 10 μm is nearly constant, equal to $0.114 ft^3/slug = 2.21 \times 10^{-4}\,\mathrm{m^3\,kg^{-1}}$. Using air density at standard temperature and pressure ($1.28\,\mathrm{kg\,m^{-3}}$) the following non-dimensional relation can be obtained between refractive index and density:

$$n - 1 = 2.8 \times 10^{-4} \times \rho/\rho_\infty. \tag{3.3}$$

Lastly, we note that in this paper the term *far field* does not necessarily mean the far field where Fraunhofer approximation is valid. However, for the default parameters the selected distance of propagation, $z_{far} - z_1$, is in the Fraunhofer far-field region with the Fresnel number of $F = a^2/(z_{far} - z_1)\lambda = 0.09 \ll 1$ (see Saleh & Teich 1991). Therefore, most of the presented results can be easily rescaled for other propagation distances as long as the target distance is within Fraunhofer limit.

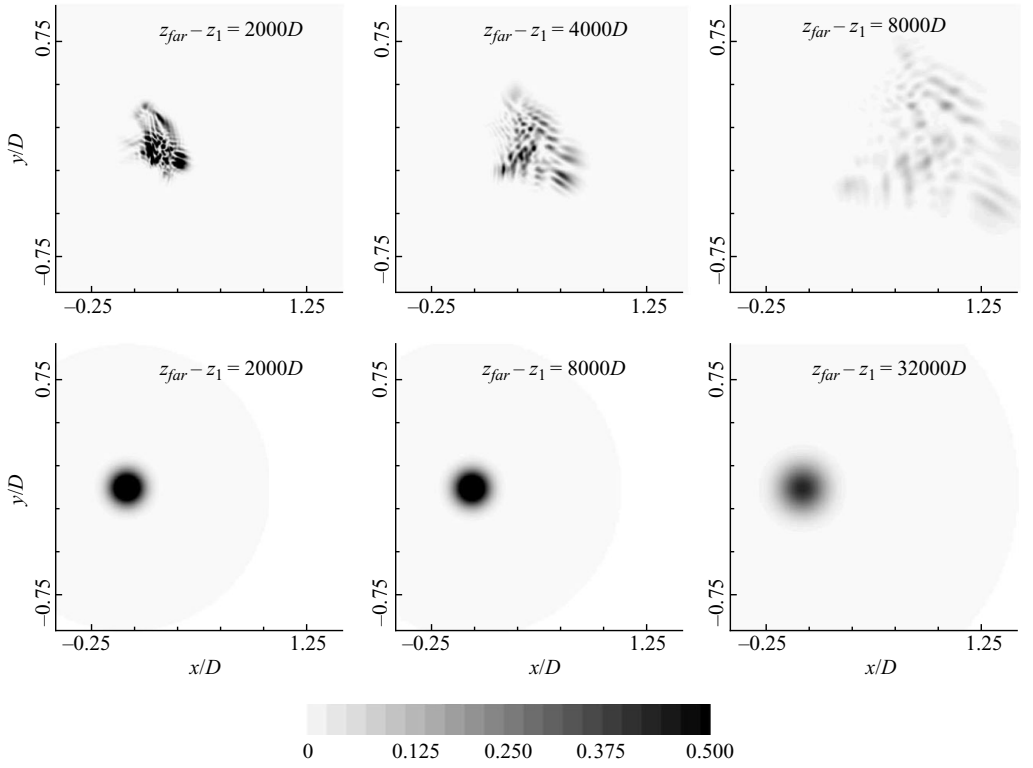

FIGURE 7. Instantaneous optical intensity patterns at different propagation distances for distorted beam (top) and undistorted beam (bottom).

4. Instantaneous results

In this section some of the optical results based on instantaneous far-field optical intensity are presented. The effect of parameters such as distance of propagation, optical wavelength and optical aperture size are shown in the example figures.

Figure 7 shows the spatial evolution of the far-field intensity of a distorted beam and contrasts it with that of an undistorted beam. Since the dimensional D is of order 1 m in relevant applications, the presented distances would be of order 1–10 km in dimensional units. While the undistorted beam remains focused for a distance of up to approximately $32\,000D$, the distorted beam starts to spread out at a distance of $4000D$. In addition, due to high-magnitude phase aberration, the distorted beam shows a highly irregular and speckled intensity pattern, as described by Zeldovich, Mamaev & Shkunov (1995).

Figure 8 shows the far-field intensity patterns for two different optical wavelengths. While the optical wavelength affects the global spread of the undistorted beam, it only affects the speckle size of the distorted beam without much changing its spread and intensity. The speckle size was found to be approximately proportional to the wavelength. Figure 9 shows a schematic explanation of this relation. When two trains of optical waves merge, an interference pattern is created. When two waves hit a z-plane with the same phase, local intensity maxima occur. Low-intensity regions correspond to out of phase interference, and the speckle size s is the distance between the adjacent peaks. Since optical wavelength determines the distance between the

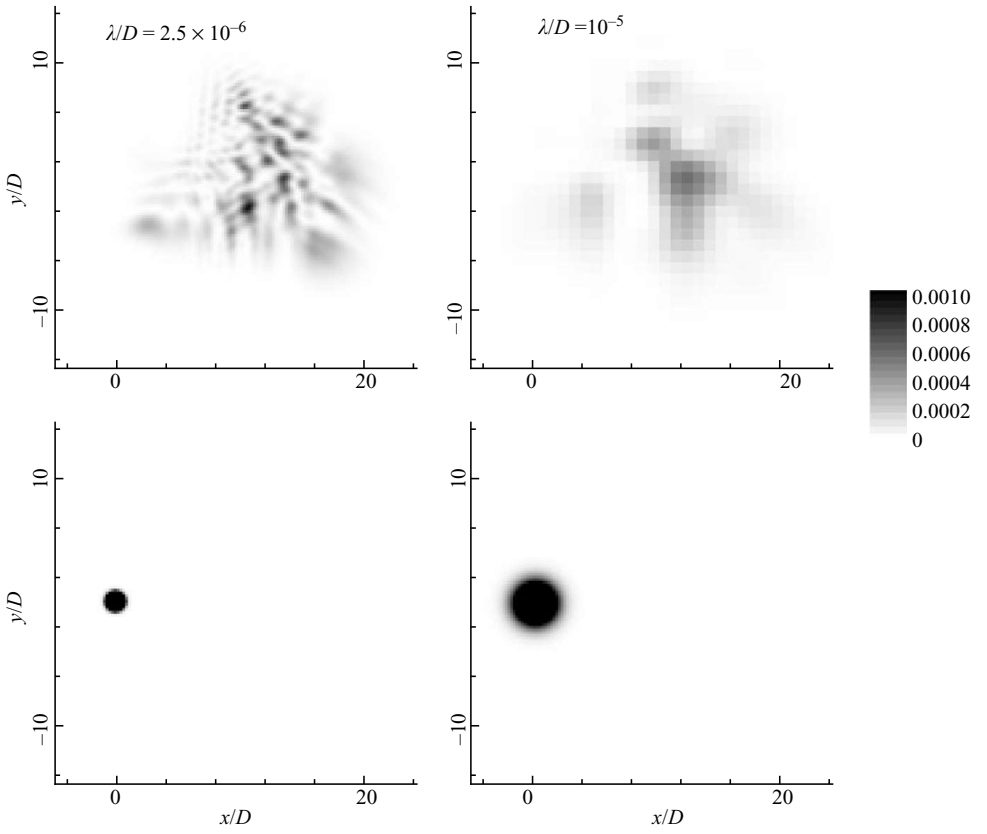

FIGURE 8. Instantaneous optical intensity for two different optical wavelengths. The top plots show the optical intensity of case 1 beam. The peak dimensionless intensity of undistorted beams are 0.074 and 0.005 for $\lambda/D = 2.5 \times 10^{-6}$ and 10^5, respectively.

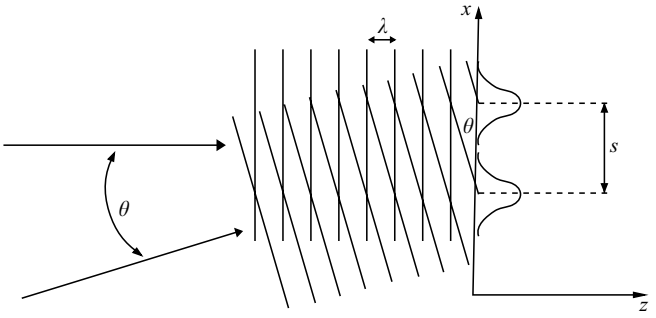

FIGURE 9. Schematics of interference. The arrows represent propagation direction, and parallel lines represent planes with the same phase which are separated by a wavelength λ. The relative scales are not realistic. At one z-location the optical intensity is plotted.

same-phase regions, it should proportionally affect the speckled pattern. Using a trigonometric relation, s can be shown to be equal to λ/θ for small θ.

Figure 10 shows the effect of optical aperture size on the instantaneous intensity pattern by comparing distortions in cases 5 and 6 (figure 5). By changing the aperture, while the spread of the beam is not changed significantly, the speckle size is changed

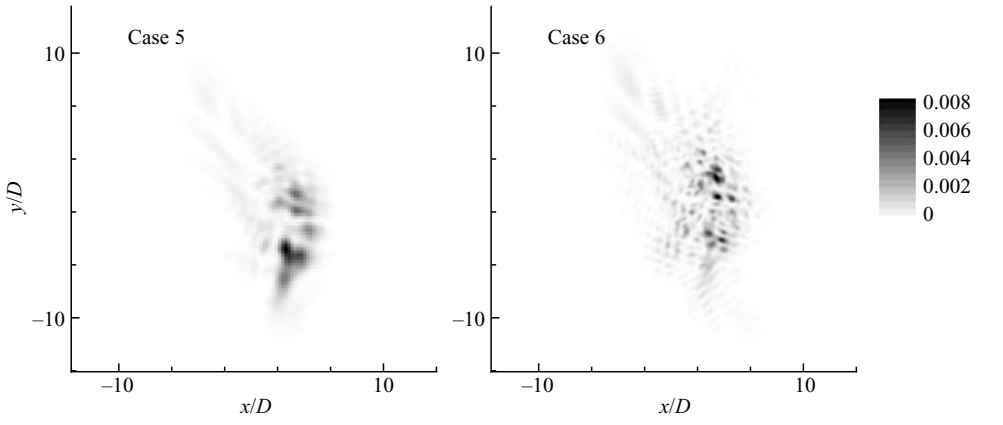

FIGURE 10. Instantaneous intensity patterns for two different aperture sizes. The plots represent the beams of cases 5 and 6. The undistorted far-filed beam intensities peak at values of 0.074 and 0.204 for case 5 and case 6, respectively.

inversely proportional to the aperture size. Again this can be explained using the interference schematic of figure 9. By tracing the rays backward in the figure, one can observe that the larger aperture allows for larger θ. In fact, θ is equal to the ratio of the aperture size to the distance of propagation. As a result, the speckle size scales as

$$s \sim \frac{\lambda}{a}(z_{far} - z_1).$$

A rough examination of our results show that this relation is valid for all of our far-field instantaneous optical computations.

The fact that the far-field optics is dominated by interference makes it difficult to find correlations between instantaneous optical intensities and local flow structures. For example, a monotonic local change in the density field may perturb the local wavefront by a distance of order wavelength, which is sufficient to cause oscillatoric changes in the far-field optical intensity (see figure 9). In other words, the change in the resulting local intensity can generate a frequency different from the flow frequency. Therefore, it is hard to detect the underlying correlation between flow and optics by simply computing cross-correlations of time series of pointwise density and pointwise far-field intensity. To avoid this problem and thereby provide a more general description of optical distortions, we study the far-field intensity through the means of spatial and temporal optical statistics. These statistics are insensitive to interference and therefore enable a cleaner examination of the link between flow structures and optical distortions.

5. Optical statistics

5.1. *Statistics based on beam moments*

As mentioned in the introduction, the wake regime is highly optically distortive. After a wavefront passes through the turbulent wake, the phase distortion is typically of order one or higher. Under such condition, the common measures of the far-field distortion of the beam, such as the SR formula introduced by Mahajan (1983) (see (1.3)), are not accurate. One approach to quantify the far-field distortion is to directly compute the far-field optical intensity patterns and their time-averaged statistics

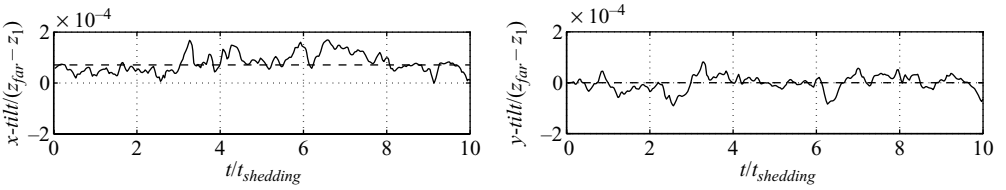

FIGURE 11. Instantaneous tilt for the beam of case 1. Beam tilt grows linearly with distance of propagation and is independent of the optical wavelength: ——, instantaneous value; – – – –, time-averaged value.

(see § 5.2). Another approach would be to quantify distortions in terms of measures introduced by Mani *et al.* (2006). Their measures directly link the far-field beam moments to the statistics of the near-field OPL defined in (1.1). We present here some of these measures with their properties, and for more details we refer the reader to Mani *et al.* (2006).

The distortion of an instantaneous optical beam can be quantified in terms of spatial moments of the far-field intensity pattern. The beam tilt in the x-direction at distance of z from aperture is defined as

$$\overline{x}(z) \equiv \frac{\iint x\ I(x, y, z)\,\mathrm{d}x\,\mathrm{d}y}{\mathscr{I}}, \tag{5.1}$$

where I is the instantaneous optical intensity (see for example figure 7) and $\mathscr{I}$ is the optical power equal to $\iint I\,\mathrm{d}x\,\mathrm{d}y$. Mani *et al.* (2006) showed that the beam tilt does not depend on the optical wavelength (assuming refractive index does not change with λ) and scales linearly with distance:

$$\overline{x}(z_{far}) = \overline{\mathscr{L}_x}(z_{far} - z_1), \tag{5.2}$$

where the bar symbol represents intensity weighted average in the x–y-plane. Here $\mathscr{L}_x$ is the x-gradient of the near-field distorted OPL, which is defined in (1.1). Note that we assumed that the x, y, z coordinates are defined such that the beam tilt before propagation is zero. The tilt in the y-direction is defined in a similar way.

Figure 11 shows the history of the x-tilt and y-tilt for the case 1 beam over 10 shedding cycles. According to the figure, the tilt distortion of the beam can reach up to 2×10^{-4} radians, which is equivalent to 2m mismatch for a 10km far field. For this beam, the tilt distortion does not vary similarly over different shedding cycles (not periodic). This is because this beam passes through a near-wake region which precedes periodic vortex shedding.

Since the flow is statistically homogeneous in the y-direction, the correlation between the y-tilt and x-tilt is expected to be zero. Using 46 shedding cycles of the tilt history we calculated this correlation to be 0.02 ± 0.09 which is statistically zero. In addition, the time-averaged y-tilt is statistically zero. The time-averaged x-tilt was computed to be $(7.0 \pm 0.4) \times 10^{-5}$ radians. We note that according to (5.2) the time-averaged tilt is proportional to the time-averaged OPL gradient which according to (1.1) would be a linear function of the density field. Since all of these relations are linear, the time-averaged tilt can be computed from the time-averaged density field. This result is only valid for tilt distortion and cannot be extended to other optical statistics.

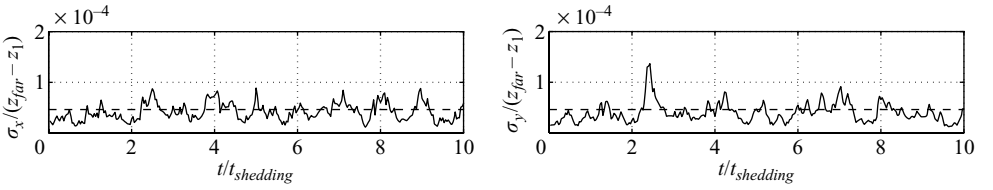

FIGURE 12. Instantaneous spread for the beam of case 1: ———, instantaneous value; – – – –, time-averaged value.

The second spatial moments of the far-field intensity represent the spreading effects of optical beams. The beam x-spread is defined as

$$\sigma_x(z) = \left(\overline{(x-\bar{x})^2}\right)^{1/2}, \tag{5.3}$$

where again the bar symbol represents intensity weighted average in the x–y-plane. Mani *et al.* (2006) obtained an exact relation for the growth of the beam spread as it propagates to the far field. Here we only present the asymptotic relation for large propagation distances (Fraunhofer limit):

$$\sigma_x^2(z_{far}) = \left(\overline{\mathscr{L}_x{}^2} - \overline{\mathscr{L}_x}^2 + \frac{\lambda^2}{4\pi^2}\overline{\left(\frac{\mathscr{A}_x}{\mathscr{A}}\right)^2}\right)(z_{far}-z_1)^2, \tag{5.4}$$

where $\mathscr{A}$ is the electromagnetic amplitude field (square root of intensity) at the aperture as defined in (3.2) and the subscript x represents partial derivative in the x-direction. According to this relation, the beam far-field spread grows linearly with the distance of propagation. Furthermore, this equation shows that the beam spread can be decomposed into two effects, a flow-induced spread (the terms involving $\mathscr{L}$) and a diffractional spread (the terms involving λ).

Figure 12 shows history of the x-spread and y-spread for the beam in case 1. The spread of undistorted beam (only diffraction term) is 2.7×10^{-6} radians and increases linearly with the wavelength. Therefore, for the case 1 beam diffraction plays a negligible role in causing beam spread. The computed time-averaged spread values are $(4.6 \pm 0.1) \times 10^{-5}$ and $(4.6 \pm 0.3) \times 10^{-5}$ in the x- and y-direction respectively. We note that the uncertainties of these numbers are due to statistical error.

From figure 12 one can qualitatively observe that there is a correlation between the beam spread in the x-direction and that in the y-direction. Based on 46 shedding cycles of the flow the cross-covariance of the plots is calculated to be 0.65 ± 0.04. This indicates that a significant portion of the optical distortion is caused by packets of three-dimensional structures. As each one of these packets pass in front of the aperture, they disperse the beam in both x- and y-direction.

Another useful instantaneous statistic is the depth of focus of the distorted beam (Δz_f), which is basically the far-field distance below which the beam's total spread($\sqrt{\sigma_x^2 + \sigma_y^2}$) does not exceed the aperture size (see Mani *et al.* 2006 for exact definition). For an undistorted beam, this definition is consistent with standard definition given by Saleh & Teich (1991). As a rule of thumb, the depth of focus is inversely proportional to the spread of the beam. Figure 13 shows the history of Δz_f for the beam of case 1. In this case, the computed time-averaged value for the depth of focus was $1930D \pm 70D$. In other words, for a 0.5m diameter cylinder, the beam

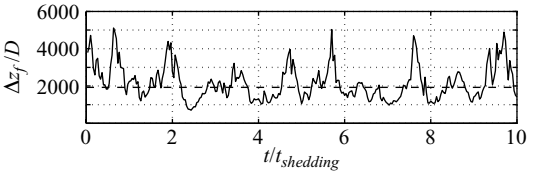

FIGURE 13. Instantaneous depth of focus for the beam in case 1: ——, instantaneous value; – – – –, time-averaged value.

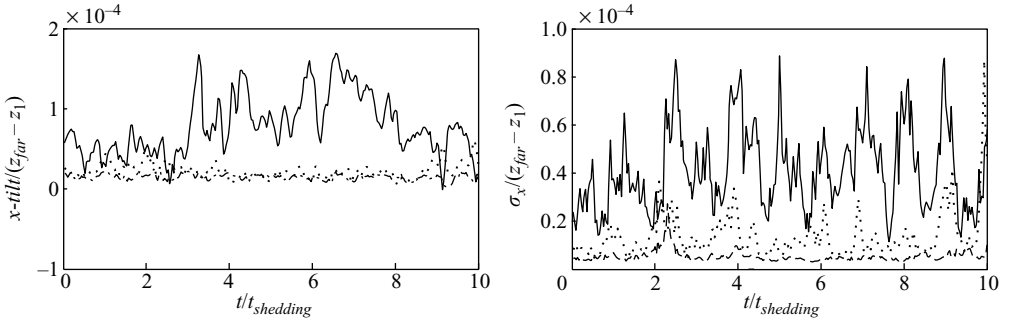

FIGURE 14. Comparison of tilt and spread for the beams of cases 1–3. The undistorted beam has a zero tilt and spread of $\sigma_x/(z_{far}-z_1)=0.027\times10^{-4}$: ——, case 1; ·····, case 2; —·—, case 3.

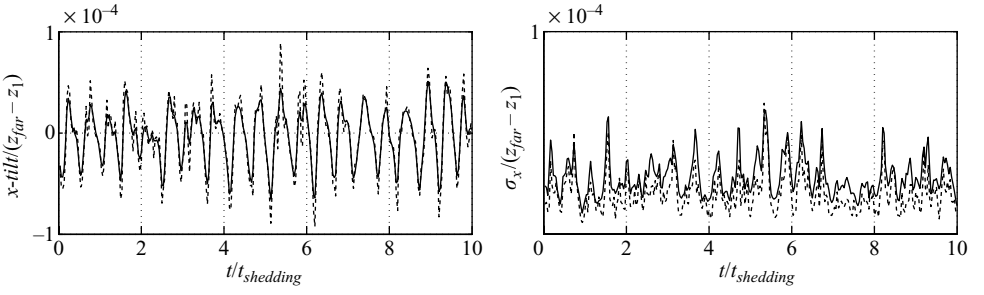

FIGURE 15. Effect of aperture size on instantaneous statistics: – – – –, case 5; ——, case 6.

is focused up to a distance of about 1 km. The focus depth of the undistorted beam is $28\,300D$ which is an order of magnitude larger than that of the distorted beam.

Figure 14 compares tilt and spread distortions for the beam cases 1, 2 and 3. As shown in figure 5, the case 1 beam passes through the separated shear layer after its transition to turbulence, while the beams of cases 2 and 3 cross the shear layer through its transitional regions. Consistently, both tilt and spread effects are lower for the case 3 beam and grow significantly as the beam angle changes towards downstream of the shear layer. The ratio of average spread distortions to spread of the undistorted beam are roughly 18, 6 and 2 for cases 1–3, respectively. In other words, as the beam shifts its angle towards the downstream region, the spread error rises by a factor of roughly three for every 17° shift. This is primarily caused by the increasing depth of the non-uniform density region passed by the beam.

Next, we examine the effect of aperture size on instantaneous optical statistics. Figure 15 shows the effect of aperture size on beam moments by comparing the

	Case 1	Case 2	Case 3	Case 4	Case 5	Case 6
OPD_{rms}/D	$(6.7 \pm 0.2) \times 10^{-6}$	1.9×10^{-6}	1.2×10^{-6}	$(5.3 \pm 0.2) \times 10^{-6}$	2.9×10^{-6}	4.9×10^{-6}
OPD_{rms}/D (Tilt-removed)	2.7×10^{-6}	0.7×10^{-6}	0.23×10^{-6}	2.2×10^{-6}	1.4×10^{-6}	3.0×10^{-6}

TABLE 3. Standard and tilt-removed time-averaged OPD r.m.s. for different cases. The uncertainty values represent statistical errors. The unreported errors are smaller than the last significant figure.

results of case 5 and case 6. The larger aperture provides a more smooth tilt time history and reduced amplitude of oscillations. This is expected, because with larger aperture the tilt is averaged over a larger flow region, and therefore there is more cancellation of fluctuations. However, the larger aperture slightly increases the spread error. With smaller aperture the beam is affected by a smaller flow region which is more coherent. Therefore, there is a higher chance that all parts of the beam are tilted in the same direction, resulting in a larger tilt and less dispersed pattern in the far field.

Another interesting observation is that the distortion history has an almost cyclic pattern for these beams. For example, one can easily detect a background shedding component in the tilt histories in figure 15. This indicates that the optically relevant density fluctuations in the downstream wake are mostly dominated by coherent vortex shedding. The frequency of optical tilt is twice the shedding frequency, since this beam is affected by vortices shed from both top and bottom of the cylinder.

5.2. *Time-averaged statistics*

In this section we present the time-averaged optical statistics for different optical configurations. We first present the commonly reported OPD r.m.s. values for each beam. OPD r.m.s. is a measure of wavefront distortion after the beam passes fluctuating refractive index field and before propagation to the far field ($z = z_1$). For each instantaneously distorted wavefront the standard definition of OPD r.m.s. is

$$OPD_{rms} = \sqrt{\overline{\left(\mathscr{L} - \overline{\mathscr{L}}\right)^2}}, \tag{5.5}$$

where the bar represents intensity-weighted spatial average in the x–y-plane and $\mathscr{L}$ is OPL, defined in (1.1). Here, in addition to standard OPD r.m.s. values, we report the tilt-removed OPD r.m.s. values. The tilt-removed OPL is defined as

$$\mathscr{L}_{tilt\text{-}removed} = \mathscr{L} - \overline{\mathscr{L}} - x\overline{\mathscr{L}_x} - y\overline{\mathscr{L}_y}. \tag{5.6}$$

The tilt-removed OPD r.m.s. is defined in a way similar to (5.5) except that instead of $\mathscr{L}$, tilt-removed OPL is used on the right-hand side. This parameter indicates the portion of OPD responsible for causing spread errors in the far field. Table 3 shows time-averaged OPD r.m.s. and the corresponding tilt-removed values for different beam cases. Considering default optical wavelength of 2.5×10^{-6}, all of the values in the table correspond to phase errors of the order unity or higher. This confirms that the SR formula does not accurately predict the far-field irradiance of these beams.

We directly computed the time series of far-field optical intensity and report time-averaged far-field statistics in figure 16 for different optical configurations. For each beam the two-dimensional intensity functions are averaged through the standard averaging method. Again, in addition to the standard average, we present the average

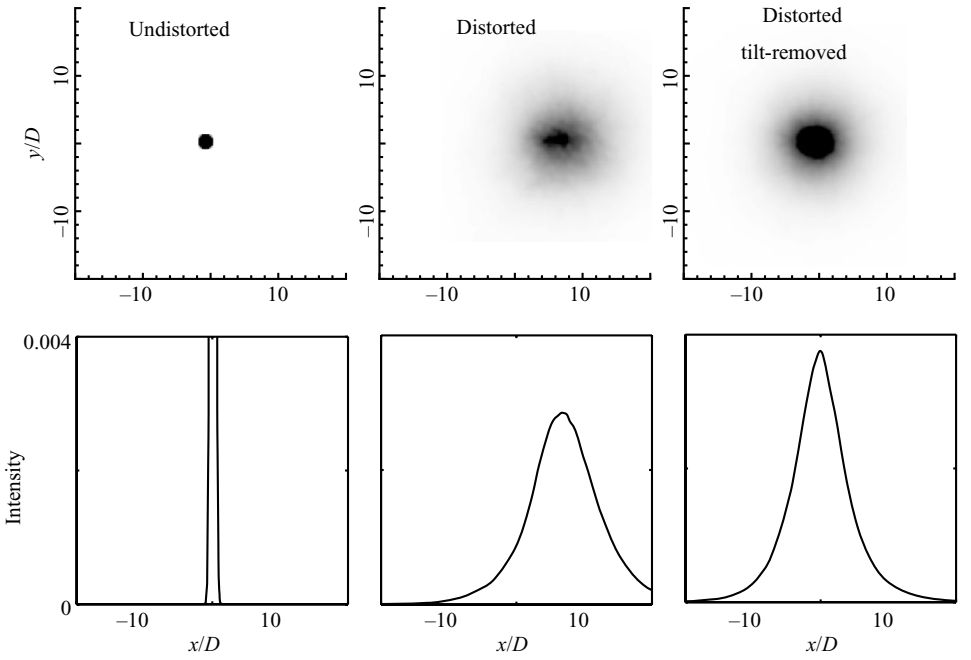

FIGURE 16. Time-averaged two-dimensional far-field beam intensity (top) and its y-integral (bottom). Shown is the data for the beam of case 1. The peak integral intensity for the undistorted beam is 0.051.

of the tilt-removed intensity. In this case, the tilt of each instantaneous optical intensity is removed by a translation in the x–y-plane before time averaging. This result represents the spread effect, while the standard averaging result shows the combined effects of both tilt and spread. To further reduce the data, we present the y-integral of these two-dimensional plots (note that y is the homogeneous flow direction) shown at the bottom of figure 16. These integral intensity values are non-dimensionalized by the product of the peak intensity of the default beam at the aperture and the cylinder diameter.

Figure 17 shows time-averaged intensities for three wavelengths in the far field for case 1 and compares them against the intensities of undistorted beams. As expected, the undistorted beams have higher intensities in the far field for each wavelength. A comparison of distorted and undistorted beams shows that only for the largest wavelength diffraction plays a significant role in causing distortion. For the two shorter wavelengths, flow-induced distortion dominates the diffraction effects. One can see that the tilt-removed peak intensity does not monotonically depend on the optical wavelength. In fact, there is an optimal wavelength that leads to a maximum time-averaged peak intensity. This optimal wavelength can be considered a useful parameter in designing optical devices. The existence of an optimal wavelength is consistent with theoretical predictions in the literature (see for example Gilbert 1982). According to these predictions, in the limit of very large wavelength, the far-field intensity drops due to diffraction effect. On the other hand, in the very short wavelength limit, the far-field intensity drops exponentially according to (1.3). Therefore an optimal wavelength must exist which delivers the maximum intensity. Note that this argument is not sufficiently general, since the SR equation is only valid for low-magnitude phase distortion.

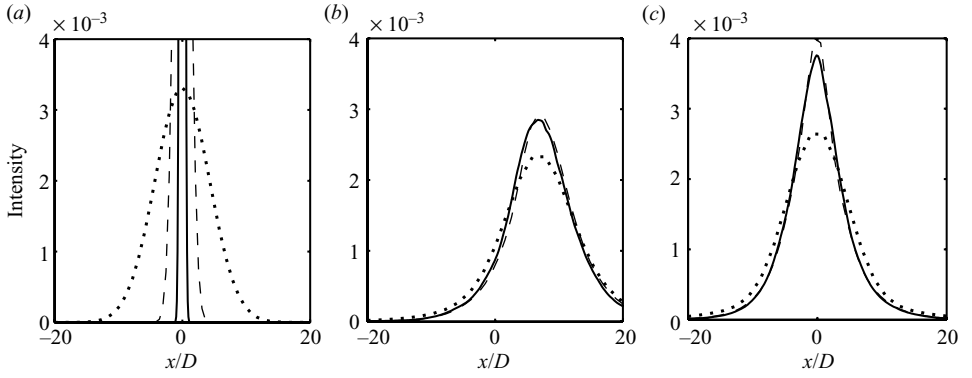

FIGURE 17. Time-averaged integral intensities of the case 1 beam for different optical wavelengths. The plots represent (*a*) undistorted beam, (*b*) standard time-averaged beam and (*c*) tilt-removed time-averaged beam. The peak intensity values for undistorted beams are 0.051, 0.013 and 0.0033 for $\lambda/D = 2.5 \times 10^{-6}$, 10^{-5} and 4×10^{-5}, respectively. The estimated statistical error of the peak values are below 4 % for all cases: ———, $\lambda/D = 2.5 \times 10^{-6}$; – – – –, $\lambda/D = 10^{-5}$; ·····, $\lambda/D = 4 \times 10^{-5}$.

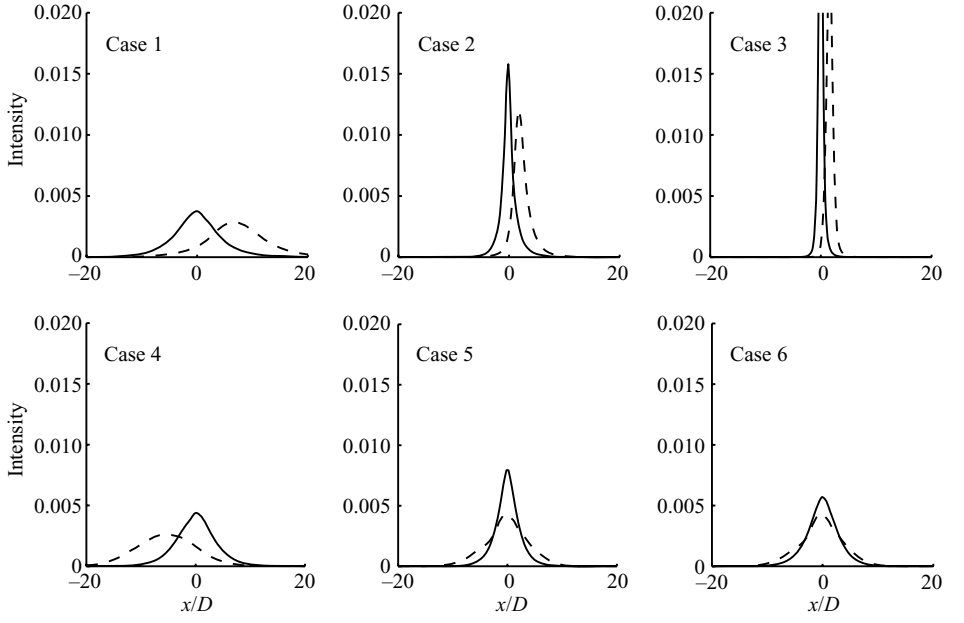

FIGURE 18. Time-averaged integral intensity for different beam cases as shown in figure 5. The peak integral intensity is 0.051 for undistorted beam and 0.032 for the beam of case 3 (tilt-removed). The estimated statistical error of the peak values are 4%, 6%, 3%, 3%, 3% and 4% for cases 1–6, respectively: – – – – standard average; ———, tilt-removed average.

Figure 18 compares the time-averaged intensities for the six different optical cases. Comparison of standard averaged plots and tilt-removed plots shows that the tilting effect is significant for all cases but is not necessarily dominant compared to the spreading effect. Consistent with the instantaneous results discussed in § 5.1, the beams in cases 2 and 3 have significantly higher far-field intensities than that of case 1. A comparison of cases 4 and 5 indicates that the near wake turbulence ($x' \sim 1.5D$)

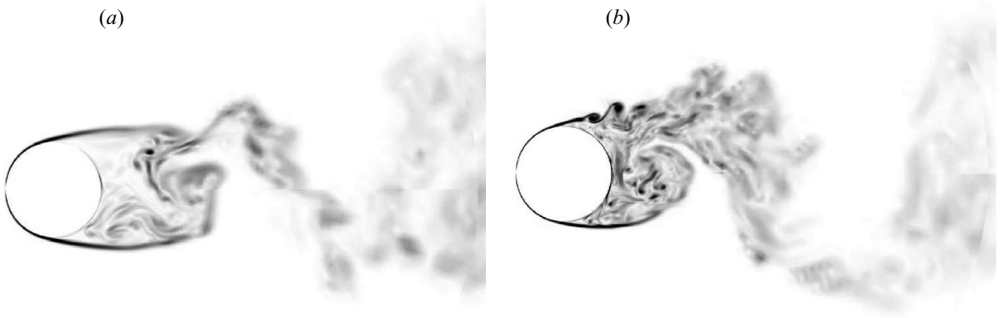

FIGURE 19. Instantaneous vorticity fields for (*a*) $Re_D = 3900$ and (*b*) $Re_D = 10\,000$. Contour levels are chosen between $0.2c_\infty/D$ and $12c_\infty/D$.

causes more distortion to the beam than the downstream turbulence ($x' \sim 3.5D$). This indicates that although the wake thickness has increased at the downstream location, turbulence intensity has decayed, which outweighs the wake growth to cause decreased optical distortion for the beam of case 5. The turbulent kinetic energy along the centreline of the wake was computed to be $0.059c_\infty^2$ at $x' = 1.5D$ (case 2) and $0.030c_\infty^2$ at $x' = 3.5D$ (case 3), where c_∞ is the free-stream speed of sound. In other words, turbulence intensity drops by a factor of two between the two stations. Figure 18 shows that the intensity of the tilt-removed beam is improved by a similar factor from case 4 to case 5.

The effect of aperture size on optical distortions can be examined by comparing the results of cases 5 and 6. The standard time-averaged intensity pattern (without tilt removal) is almost the same for both apertures. In other words the combined tilt and spread effects are the same for both beams. We note that although the larger aperture beam has better diffraction properties, this effect has not caused much improvement due to dominance of flow-induced distortion. Consistent with the results in § 5.1, smaller aperture beam has better spread property and worse tilt effect than larger aperture beam.

6. The effect of laminar versus transitional shear layers

In this section we compare optical distortion caused by flow at two different Reynolds numbers. Using the same numerical method described in § 2, we performed LES of turbulent flow over a cylinder at Reynolds number 10 000. Due to this *Re* increase, in addition to developing more small structures in the wake, the separated shear layers experience a significant change of state from laminar to transitional with distinct coherent vortices.

Figure 19 compares the instantaneous vorticity fields of the two flows. In the lower Reynolds number case, the separated shear layer breaks down by Kármán instability while in the high-*Re* case Kármán instability is preceded by Kelvin–Helmholtz instability. In this case, the separated shear layer breaks down earlier, and the point of transition is moved upstream. This effect can be explained by examining the effect of Reynolds number on relative growth rate of the two instabilities. While the wake size and thus Kármán instability characteristics are not much affected by the Reynolds number, the higher *Re* flow develops thinner shear layers. This increases the growth rate of the Kelvin–Helmholtz instability (see Ho & Huerre 1984 for example) and causes appearance of its corresponding structures before shedding occurs. This

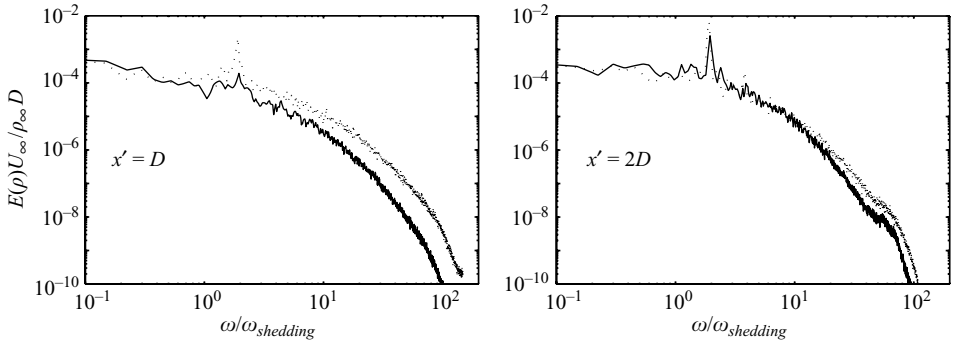

FIGURE 20. Effect of Reynolds number on the density spectra at wake centreline locations. Non-dimensional frequencies are normalized by the Strohal number of the $Re_D = 3900$ case: ———, $Re_D = 3900$; ·····, $Re_D = 10\,000$.

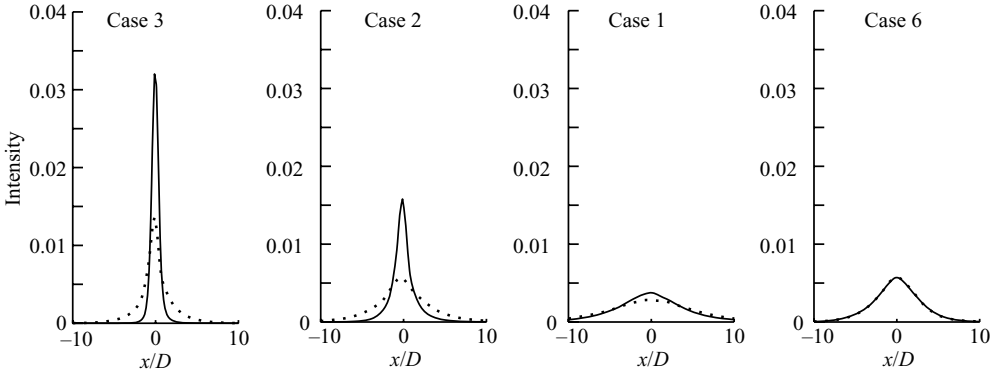

FIGURE 21. Effect of Reynolds number on beam distortions: the plots represent average tilt-removed integral intensity for different beam cases. The peak integral intensity for undistorted beam is 0.051, and the statistical errors of $Re = 10\,000$ plots are 4%, 10%, 11% and 4% for cases 3, 2, 1, and 6, respectively: ———, $Re_D = 3900$; ·····, $Re_D = 10\,000$.

observation is consistent with the result of Dong *et al.* (2006) for incompressible turbulent flow over a cylinder at the same Reynolds numbers. For more details on transition of flow over cylinder see the book by Zdravkovich (1997). It can also be seen in the figure 19 that after the shedding instability in the wake both *Re* cases have qualitatively similar large-scale structures.

Figure 20 shows density spectra at the centreline of the wake for the two Reynolds numbers. In the very near wake, at $x = 1D$ the higher Reynolds number flow contains higher fluctuations at all frequencies. This is expected, since this location is close to the transitional region. However further downstream, at $x = 2D$, the spectra of both flows are almost the same except at high frequencies. This indicates that the effect of initial transition on turbulence diminishes as flow evolves and convects downstream.

Figure 21 compares time-averaged optical intensities for the two Reynolds numbers for optical beams of cases 1–3 and 6. One observes that for the beams which pass through the transitional flow regimes (i.e. cases 2 and 3), changing *Re* significantly affects the far-field optical intensity. The beam of case 1 which passes through the near wake after its transition to turbulence is much less affected by the change in *Re*. The case 6 beam is almost unaffected although the higher Reynolds number flow has

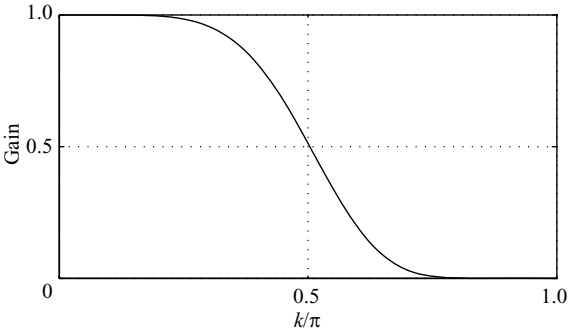

FIGURE 22. Fourier transform of the low-pass filter used to obtain coarser representation of the density field.

higher density fluctuations at high frequencies. This indicates that the corresponding small-scale turbulent structures are optically unimportant as observed by Zubair & Catrakis (2007) and described by Mani, Wang & Moin (2008).

In summary, for the case of developed turbulence, where increasing Reynolds number only affects the high-frequency spectra, optical distortions are not sensitive to Reynolds number. In contrast, in the transitional regimes, Reynolds number can significantly alter flow character which consequently influences optical distortions. In these observations the shear layer thickness, which is influenced by the Reynolds number, plays an important role in altering the flow regime. In practical applications where Reynolds numbers of the order 10^7 are encountered, the thickness and dynamic regime of the shear layer should be captured accurately for aero-optical predictions. In these flows transition to turbulence occurs before separation of the shear layer (assuming $Re > 10^6$). Therefore, it is expected that changing Re would not significantly alter the separated shear layer regime and only influences the small scales which are optically less important.

7. Effect of small flow structures

In this section we examine the effect of small flow scales on optical distortions by comparing optical distortions caused by flows represented with different resolution. Since higher Reynolds number flows involve smaller flow structures, we only present this study for the higher Reynolds number case.

In the first step, we used a low-pass numerical filter to filter the density field obtained from the original LES simulation. The transfer function of this sixth-order filter is shown in figure 22. The filter was obtained by five repeated operations of the following transformation in each direction:

$$\hat{f}_i = \frac{11}{16} f_i + \frac{15}{64}(f_{i+1} + f_{i-1}) - \frac{3}{32}(f_{i+2} + f_{i-2}) + \frac{1}{64}(f_{i+3} + f_{i-3}). \tag{7.1}$$

This filter provides a coarser representation of the flow in each direction by about a factor of two. By comparing the optical results for the beams passing through the filtered flow with the unfiltered results we can evaluate the effect of small flow structures on optical distortions.

Furthermore, we performed a grid refinement study of the flow to ensure that all of the relevant flow scales are captured by LES. An additional flow simulation was performed in which the resolution was doubled in each direction compared to the

Density source data	Equivalent resolution
Coarse (original) simulation	$288 \times 396 \times 48$
Original simulation filtered	$144 \times 198 \times 24$
Fine simulation	$576 \times 792 \times 96$
Fine simulation filtered	$288 \times 396 \times 48$

TABLE 4. Test cases used for grid convergence study of optical computations at $Re = 10\,000$.

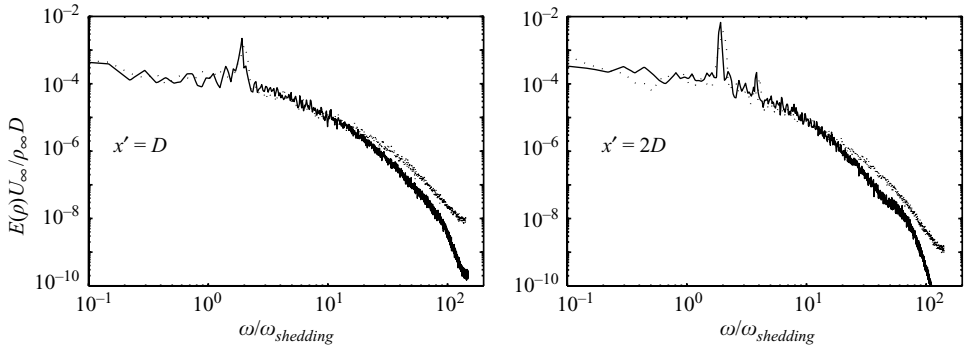

FIGURE 23. Effect of grid resolution on the density spectra at two wake centreline locations. The spectra are obtained for flow at $Re = 10\,000$ and $M = 0.4$: ———, coarse mesh; ·····, fine mesh.

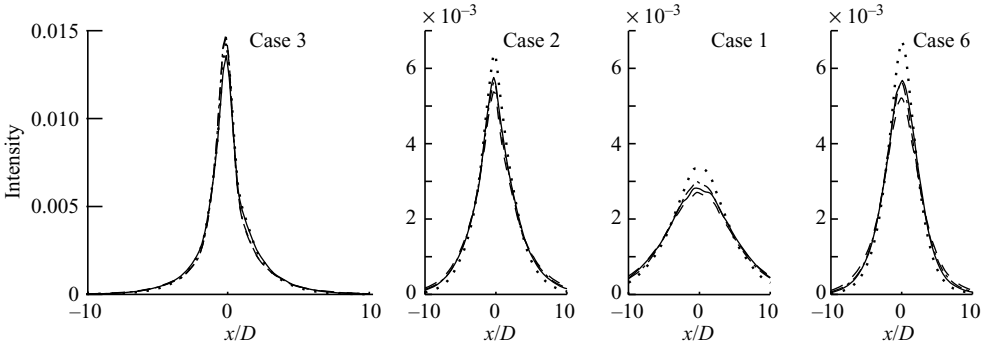

FIGURE 24. Effect of flow resolution on optical computations; the plots represent average tilt-removed integral intensity for different beam cases: ——— coarse (original) simulation; ····· coarse simulation filtered; – – – – fine simulation; —·— fine simulation filtered.

original simulation. The optical results of this fine LES were compared with the results of the original simulation. In addition, the density field of this flow was filtered to obtain a resolution comparable to the original resolution. By a combination of filtering and grid refinement we obtained density fields at three different resolution levels as presented in table 4. Figure 23 compares the density spectrum of the coarse mesh simulation (original LES) with that of fine mesh simulation. The spectra of both cases are similar except for high frequencies where the finer simulation has captured more energy than the original LES.

The time-averaged optical results of these flow fields are shown in figure 24. Except for the coarsest representation of the flow (coarse simulation filtered), all other

plots are in agreement within statistical error. Therefore, it appears that the original simulation has sufficient resolution to capture the optically relevant scales. Coarser representation (than the original LES) of the flow can lead to up to 20 % error in optical computations.

8. Conclusion

In summary, high-resolution large eddy simulations of compressible flow past a circular cylinder at $Re_D = 3900$ and 10 000 and $M = 0.4$ were performed, and the flow statistics have been validated against previous experimental and numerical results. Using the space–time history of the refractive index (density) field from LES, instantaneous and statistical descriptions of the flow-induced optical aberrations have been studied for different optical wavelengths, aperture sizes and beam positions in the flow.

Our results show that the turbulent wake flow can significantly degrade the performance of optical beams. In the range of relevant optical wavelengths, the maximum irradiance of the optical beam can be reduced by one or two orders of magnitude. Also, turbulence can severely limit the effective range of an optical beam. It was observed that while the instantaneous optical intensity is strongly affected by the beam's wavelength, optical statistics are less affected by changing this parameter. Unlike the undistorted case where shorter wavelengths are desirable for greater depth of focus, for propagation through an aberrating medium, there is an optimal wavelength. In addition to the turbulent wake, coherent vortices in the unstable shear layers also lead to significant distortions of optical beams.

Through comparison of flows at two Reynolds numbers, optical distortions by the downstream wake are found to be insensitive to Reynolds number. However, because the instability and transition of the separated shear layer is affected at this Reynolds number range, the near wake is found to cause more distortions for $Re_D = 10\,000$ than $Re_D = 3900$. By changing the optical aperture size and also filtering the flow, the optical effects of different flow scales were studied, and through a grid convergence study it was confirmed that the present LES captures all of the optically relevant flow scales.

This work was supported by the Air Force Office of Scientific Research under grant numbers F49-620-03-1-0132 and FA9550-06-1-0147. Ali Mani is supported by a Charles H. Kruger Stanford Graduate Fellowship. Computer time was provided by NAS at NASA Ames Research Center.

REFERENCES

Beaudan, P. & Moin, P. 1994 Numerical experiments on the flow past a circular cylinder at sub-critical Reynolds number. *Tech Rep*. TF-62. Department of Mechanical Engineering, Stanford University.

Cassady, P. E., Birch, S. F. & Terry, P. J. 1989 Aero-optical analysis of compressible flow over an open cavity. *AIAA J*. 758–762.

Catrakis, H. J. & Aguirre, R. C. 2004 New interfacial fluid thickness approach in aero-optics with applications to compressible turbulence. *AIAA J*. **42**, 1973–1981.

Catrakis, H. J., Aguirre, R. C., Ruiz-plancarte, J., Thayne, R. D., McDonald, B. A. & Hearn, J. W. 2002 Large-scale dynamics in turbulent mixing and the three-dimensional space–time behavior of outer fluid interfaces. *J. Fluid Mech*. **471**, 381–408.

Childs, R. E. 1993 Prediction and control of turbulent aero-optical distortion using large eddy simulation. Paper 93-2670. AIAA.

Dimotakis, P. E., Catrakis, H. J. & Fourguette, D. C. 2001 Flow structure and optical beam propagation in high-Reynolds number gas-phase shear layer and jets. *J. Fluid Mech.* **433**, 105–134.

Dong, S., Karniadakis, G. E., Ekmekci, A. & Rockwell, D. 2006 A combined direct numerical simulation–particle image velocimetry study of the turbulent near wake. *J. Fluid Mech.* **569**, 185–207.

Freeman, A. P. & Catrakis, H. J. 2008 Direct reduction of aero-optical aberrations by large structure suppression control in turbulence. *AIAA J.* **46**, 2582–2590.

Gilbert, K. G. 1982 Overview of aero-optics. (ed. K. Gilbert and L. J. Otten) In *Progress in Astronautics and Aeronautics: Aero-Optical Phenomena*, American Institute of Aeronautics and Astronautics, New York, N.Y. vol. 80, pp. 1–9.

Gordeyev, S., Jumper, E. J., Ng, T. T. & Cain, A. B. 2003 Aero-optical characteristics of compressible, subsonic turbulent boundary layers. Paper 2003-3606. AIAA.

Ho, C. M. & Huerre, P. 1984 Perturbed free shear layers. *Annu. Rev. Fluid Mech.* **16**, 365–424.

Hugo, R. J., Jumper, E. J., Havener, G. & Stepanek, C. 1997 Time-resolved wave front measurements through a compressible free shear layer. *AIAA J.* **35**, 671–677.

Jones, M. I. & Bender, E. E. 2001 CFD-based computer simulation of optical turbulence through aircraft flowfields and wakes. Paper 2001-2798. AIAA.

Kravchenko, A. G. & Moin, P. 1998 B-spline methods and zonal grids for numerical simulations of turbulent flows. *Tech Rep.* TF-73. Department of Mechanical Engineering, Stanford University.

Kravchenko, A. G. & Moin, P. 2000 Numerical studies of flow over a circular cylinder at $Re_D = 3900$. *Phys. Fluids* **12**, 403–417.

Lilly, D. K. 1992 A proposed modification of the Germano subgrid-scale closure method. *Phys. Fluids* A **4**, 633–635.

Mahajan, V. N. 1983 Strehl ratio for aberration in terms of their aberration variance. *J. Opt. Soc. Am.* **73**, 860–861.

Malley, M., Sutton, G. W. & Kincheloe, N. 1992 Beam-jitter measurements of turbulent aero-optical path differences. *Appl. Opt.* **31**, 4440–4443.

Mani, A., Wang, M. & Moin, P. 2006 Statistical description of free-space propagation for highly aberrated optical beams. *J. Opt. Soc. Am.* A **23**, 3027–3035.

Mani, A., Wang, M. & Moin, P. 2008 Resolution requirements for aero-optical simulations. *J. Comput. Phys.* **227**, 9008–9020.

Mittal, R. & Moin, P. 1997 Suitability of upwind-biased finite-difference schemes for large-eddy simulation of turbulent flows. *AIAA J.* **35**, 1415–1417.

Moin, P., Squires, K., Cabot, W. & Lee, S. 1991 A dynamic subgrid-scale model for compressible turbulence and scalar transport. *Phys. Fluids* A **3**, 2746–2757.

Nagarajan, S., Lele, S. K. & Ferziger, J. H. 2003 A robust high-order compact method for large eddy simulation. *J. Comput. Phys.* **191**, 392–419.

Ong, L. & Wallace, J. 1999 The velocity field of the turbulent very near wake of a circular cylinder. *Exp. Fluids* **20**, 441–453.

Press, W. H., Teukolsky, S. A., Vetterling, W. T. & Flannery, B. P. 2007 *Numerical Recipes: The Art of Scientific Computing*. Cambridge University Press.

Rizzetta, D. P., Visbal, M. R. & Blaisdell, G. A. 2003 A time-implicit high-order compact differencing and filtering scheme for large-eddy simulation. *Intl J. Numer. Methods Fluids* **42**, 665–693.

Saleh, B. E. A. & Teich, M. C. 1991 *Fundamentals of Photonics*. John Wiley & sons.

Sinha, N., Arunajatesan, S., Seiner, J. M. & Ukeiley, L. S. 2004 Large-eddy simulations of aero-optic flow fields and control application. Paper 2004-2448. AIAA.

Smith, R. & Truman, C. 1990 Prediction of optical phase degradation using a turbulent transport equation for the variance of index-of-refraction fluctuations. Paper 90-0250. AIAA.

Sutton, G. W. 1969 Effect of turbulence fluctuations in an optically active fluid medium. *AIAA J.* **7**, 1737–1743.

Sutton, G. W. 1985 Aero-optical foundations and applications. *AIAA J.* **23**, 1525–1537.

Tromeur, E., Garnier, E. & Sagaut, P. 2006 Large eddy simulations of aero-optical effects in a spatially developing turbulent boundary layer. *J. Turbul.* **7** (001).

Tromeur, E., Garnier, E., Sagaut, P. & Basdevant, C. 2003 Large eddy simulations of aero-optical effects in a turbulent boundary layer. *J. Turbul.* **4** (005).

Truman, C. R. 1992 The influence of turbulent structure on optical phase distortion through turbulent shear flows. Paper 92-2817. AIAA.

Truman, C. R. & Lee, M. J. 1990 Effects of organized turbulence structures on the phase distortion in a coherent optical beam propagating through a turbulent shear flow. *Phys. Fluids* A **2**, 851–857.

Tsai, Y. P. & Christiansen, W. H. 1990 Two-dimensional numerical simulation of shear-layer optics. *AIAA J.* **28**, 2092–2097.

Visbal, M. R. & Rizzetta, D. P. 2008 Effect of flow excitation on aero-optical aberration. Paper 2008-1074. AIAA.

Wolfe, W. L. & Zizzis, G. J. 1978 *The Infrared Handbook*. Office of Naval Research, Department of the Navy.

Zdravkovich, M. M. 1997 *Flow around Circular Cylinders*. Oxford University Press.

Zeldovich, B. Y., Mamaev, A. V. & Shkunov, V. V. 1995 *Speckle-wave Interactions in Application to Holography and Nonlinear Optics*. CRC Press.

Zubair, F. R. & Catrakis, H. J. 2007 Aero-optical resolution robustness in turbulent separated shear layers at large Reynolds numbers. *AIAA J.* **45**, 2721–2728.